Review

Precise Vapor-Phase Synthesis of Two-Dimensional Atomic Single Crystals

Shasha Zhao,[1,2] Luyang Wang,[1,2] and Lei Fu[1,*]

Two-dimensional atomic single crystals (2DASCs) have drawn immense attention because of their potential for fundamental research and new technologies. Novel properties of 2DASCs are closely related to their atomic structures, and effective modulation of the structures allows for exploring various practical applications. Precise vapor-phase synthesis of 2DASCs with tunable thickness, selectable phase, and controllable chemical composition can be realized to adjust their band structures and electronic properties. This review highlights the latest advances in the precise vapor-phase synthesis of 2DASCs. We thoroughly elaborate on strategies toward the accurate control of layer number, phase, chemical composition of layered 2DASCs, and thickness of non-layered 2DASCs. Finally, we suggest forward-looking solutions to the challenges and directions of future developments in this emerging field.

INTRODUCTION

Two-dimensional (2D) materials have aroused widespread attention with excellent electronic, optical, magnetic properties, and extensive application prospect owing to the quantum confinement effect. However, grain boundaries in 2D films could degrade their mechanical and electrical behaviors (Yazyev and Louie, 2010). Two-dimensional atomic single crystals (2DASCs) can avoid these issues and are valuable for their future studies and practical applications in optics and electronics. Layered 2DASCs with strong covalent bonds in each atomic layer and weak van der Waals (vdW) interactions between the layers exhibit layer-dependent properties (Huang et al., 2017; Ciarrocchi et al., 2018; Wang et al., 2017), whereas non-layered 2DASCs with intrinsic covalent bonds may bring up more exotic properties and advanced functionalities that cannot be achieved in higher dimensionalities. Additionally, different phases and chemical compositions of 2DASCs have a great influence on their electronic structures and properties. From this point of view, precise synthesis of 2DASCs is necessary for exploring the structure-property correlations and further achieving the modulation of properties as expected. Herein, "precise synthesis" denotes that the thickness, phase, and chemical composition of 2DASCs would be well regulated during the synthesis process. Recently, researchers have made significant breakthroughs in the precise vapor-phase synthesis of 2DASCs in scalable and controllable ways, which are illustrated in Tables 1, 2, 3, and 4. Herein, we give a comprehensive review of the recent developments in the precise synthesis of 2DASCs. We elaborate on the fundamental growth mechanism of 2DASCs and discuss the strategies toward the accurate control of layer number, phase, chemical composition of layered 2DASCs, and thickness of non-layered 2DASCs. We also list several key challenges and opportunities in the precise vapor-phase synthesis of 2DASCs and suggest the solutions to further promote developments in this important field.

GROWTH MECHANISM OF 2DASCS

In-depth understanding of the growth mechanism of 2DASCs is instructive to regulate their growth process. In general, vapor-phase growth of 2DASCs involves three essential steps: evaporation and thermal decomposition of precursors; transport and migration of reactants; nucleation and growth of crystals.

Evaporation and Thermal Decomposition of Precursors

The supply of reactants for the subsequent adsorption and surface reaction on the substrate originates from the evaporation or thermal decomposition of precursors, which is dependent on the state of precursors. Solid precursors initially evaporate when heated in the source zone. Both the melting point of precursors and the source zone temperature will affect this process. Decreasing their melting point can contribute to the evaporation and the release of reactant atoms or clusters. Taking the growth of transition metal

[1]College of Chemistry and Molecular Sciences, Wuhan University, Wuhan 430072, China

[2]These authors contributed equally

*Correspondence: leifu@whu.edu.cn

Layered 2DASCs	Synthesis Method	Layer Number	Domain Size	Reference
Graphene	CVD on Cu	Monolayer Bilayer	5.0 mm 300.0 μm	Zhou et al., 2013
	CVD on Cu	Bilayer	300.0–550.0 μm	Hao et al., 2016
h-BN	CVD on Cu	Monolayer 1.0 nm	35.0 μm^2	Tay et al., 2014
	CVD on Fe/SiO$_2$/Si	Monolayer <0.4 nm	0.3 mm	Caneva et al., 2015
	CVD on Cu–Ni alloy	Monolayer 0.4 nm	7,500.0 μm^2	Lu et al., 2015
Antimonene	VdWE on mica	10 atomic layers 4.0 nm	5.0–10.0 μm	Ji et al., 2016

Table 1. Summary of Single Crystals of Graphene, h-BN, and Antimonene

dichalcogenides (TMDs) as an example, molten salts (NaCl, KCl, etc.) can reduce the melting point of precursors to promote their evaporation (Manukyan et al., 2011; Li et al., 2015; Gaune-Escard and Haarberg., 2014). A library of 2D TMDs has been successfully synthesized by molten-salt-assisted chemical vapor deposition (CVD) (Zhou et al., 2018). Besides, high source zone temperature can also accelerate the evaporation by increasing the saturation pressure of gasified precursors. For gaseous precursors, thermal decomposition initially occurs. The formation and population of the active species are influenced by the catalytic ability of the substrate and source zone temperature (Wu et al., 2014; Abild-Pedersen et al., 2007). The melting point of precursors should be appropriate to maintain a continuous precursor supply. In addition, the chemical reactivity of precursors should be high and the electronegativity differences between precursors should be large to ensure chemical reaction between them.

Transport and Migration of Reactants

Mass transport is realized via the diffusion of gaseous reactants from the source zone to the growth zone. Transport agent in chemical vapor transport (CVT) and carrier gas in CVD serve as transport medium, respectively. In the CVT process, based on Schafer's transport equation, the transport rate J can be described (Köppe et al., 2003) as:

$$J \propto \frac{P_i}{\sum P_i} \cdot \frac{s}{l} \cdot \overline{T}^{-0.75}$$

where P_i is the partial pressure of the effective species, which relies on the amounts of transport agent; s and l are the cross section and length of the diffusion path, respectively; and $\overline{T}$ is the average temperature of the source zone and the growth zone. Therefore, to slow down the mass transport rate and enable the growth of 2DASCs in the CVT process (Wang et al., 2016), we should minimize the concentration of transport agents or reactants, increase the length of diffusion while decrease the cross section of the diffusion path, and reduce the average temperature. The transport capability of a suitable transport agent should be low to reduce the growth rate of 2DASCs (Wang et al., 2016). I$_2$ is the most widely used for conventional CVT growth. However, it is not feasible for the growth of ultrathin TiSe$_2$ owing to its relatively high transport ability. AgCl is suitable for the growth of 2D TiSe$_2$ as it decomposes to produce Cl$_2$ at a suitable temperature, allowing for slow mass transport (Wang et al., 2016). As for the CVD growth, tuning the flow rate of carrier gas is crucial to control the mass flux, further influencing the mass transfer process. In the CVD process, low flow rate causes a relatively slow mass transfer process, whereas high flow rate leads to a fast mass transfer rate (Li et al., 2018).

When the reactant atoms reach the substrate surface, they are captured by the substrate as adatoms. The adatoms will migrate along the surface, and the migration coefficient (D_m) can be expressed as:

$$D_m \propto e^{-\frac{E_m}{kT}}$$

where k is the Boltzmann constant, T is the substrate temperature, and E_m is the migration barrier energy of adatoms (Cheng et al., 2017). According to the above-mentioned formula, the migration rate of adatoms is

Layered 2DASCs	Synthesis Method	Phase/Crystal Structure	Electronic Characteristics	Layer Number	Domain Size	Reference
MoS$_2$	CVT on mica	2H	Semiconductor 1.86 eV	Monolayer 0.80 nm	30.00–60.00 µm	Hu et al., 2017
	LPCVD on soda-lime glass	2H	Semiconductor 1.88 eV	Monolayer 0.77 nm	400.00 µm	Yang et al., 2018
	K-assisted CVD on mica	1T' 2H	Metal (1T') Semiconductor (2H) 1.83 eV	Monolayer 0.90 nm (1T') 0.70 nm (2H)	–	Liu et al., 2018
	Reverse-flow CVD on SiO$_2$/Si	2H (AB) 3R (AA)	Semiconductor 1.80 eV	Bilayer 1.40 nm	300.00 µm	Zhang et al., 2019
MoSe$_2$	CVD on molten glass	2H	Semiconductor 1.29 eV	Monolayer 0.97 nm	2.50 mm	Chen et al., 2017
MoTe$_2$	Iodine mediated CVD on SiO$_2$/Si	1T'	–	Monolayer 1.00 nm	46.90 µm	Zhang et al., 2017
	CVD on SiO$_2$/Si	1T'	–	Monolayer 0.80 nm	–	Naylor et al., 2016
	CVD on various substrates	1T' 2H	Semiconductor 1.10 eV (2H)	Few layers (5.00–6.00 nm)	A few tens of micrometers	Sung et al., 2017
	CVD on SiO$_2$/Si	1T'	Semimetal	Monolayer	1.00 mm	Chen et al., 2017
	VdWE on mica	3R	Semiconductor 1.00 eV	9.00 nm	–	Yang et al., 2018
WTe$_2$	CVD on SiO$_2$/Si	1T'	Semimetal	Monolayer	350.00 µm	Chen et al., 2017
WS$_2$	CVD on Au	2H	Semiconductor 2.02 eV	Monolayer 0.95 nm	Millimeter-size	Gao et al., 2015
WSe$_2$	Cu-assisted self-limited CVD on W film	2H	Semiconductor 1.63 eV	Monolayer 0.73 nm	1.33 mm^2 s^{-1}	Liu et al., 2016
TiSe$_2$	CVT on sapphire	1T	Metal	3.00–8.00 nm	4.00–10.00 µm	Wang et al., 2016
ZrS$_2$	LPCVD on h-BN	1T	Semiconductor	Monolayer 1.00 nm	1.00–3.00 µm	Zhang et al., 2015
HfS$_2$	VdWE on mica	1T	Semiconductor 1.45 eV	Monolayer 0.68 nm	–	Fu et al., 2017
HfSe$_2$	CVD on c-plane sapphire	1T	Semiconductor 1.94 eV	Monolayer 0.62 nm	–	Wang et al., 2018
TaS$_2$	CVD on Au	2H	Semiconductor	15.00 nm	20.00 µm	Shi et al., 2017
TaSe$_2$	CVD on Au	2H	Metal	Monolayer 0.80 nm	3.00–20.00 µm	Shi et al., 2018
ReSe$_2$	CVD on Au	1T	Semiconductor 1.20 eV	Monolayer 0.90 nm	2.00–20.00 µm (long edge)	Jiang et al., 2018
NiTe$_2$	CVD on SiO$_2$/Si	1T	Metal	Monolayer to multilayers 0.90, 1.60, 2.30, 2.90, 3.50, 4.10, 4.80 nm	5.00–440.00 µm	Zhao et al., 2018

Table 2. Summary of Other Layered 2DASCs

Layered 2DASCs	Synthesis Method	Phase/Crystal Structure	Electronic Characteristics	Layer Number	Domain Size	Reference
PtSe$_2$	CVT on mica	1T	1.70 eV (1L), 0.52 eV (2L), 0.13 eV (3L)	1–20 layers	10.00–50.00 μm	Hu et al., 2019
PtTe$_2$	CVD on SiO$_2$/Si	1T	Semimetal	1.80–20.00 nm	80.00 μm	Ma et al., 2018
SnS$_2$	CVD on SiO$_2$/Si	Hexagonal	Semiconductor 2.77 eV	1.10 nm	–	Ahn et al., 2015
SnSe$_2$	VdWE on mica	–	Semiconductor 1.73 eV	Bilayer 1.50 nm	40.00 μm	Zhou et al., 2015
Cu$_2$S	Super-cooling CVD on SiO$_2$/Si	β	–	Bilayer 1.80 nm	20.00 μm	Li et al., 2015
GaSe	VdWE on mica	Hexagonal	Semiconductor	Monolayer 0.80 nm	Tens of micrometers	Zhou et al., 2014
	Vapor phase mass transport on SiO$_2$	–	Semiconductor 3.30 eV	Two or three layers 2.00 nm	Tens of micrometers	Lei et al., 2013
InSe	VdWE on mica	ε hexagonal γ rhombohedral	Semiconductor 2.40 eV (one layer) 1.92 eV (two layers)	Monolayer 0.84 nm	250.00 μm	Chang et al., 2018
CoSe	CVD on SiO$_2$/Si	Tetragonal	Metal	2.30 nm	20.00 μm	Ma et al., 2019
SnS	CVD on SiO$_2$/Si	Orthorhombic	Semiconductor 1.26 eV	12.10 nm	–	Ahn et al., 2015
SnSe	VdWE on mica	Orthorhombic	Semiconductor	6.00–40.00 nm	1.00–6.00 μm	Zhao et al., 2015
In$_2$S$_3$	VdWE on mica	β Tetragonal (defective spinel)	Semiconductor 2.02 eV	1.50 nm	10.00 μm	Huang et al., 2017
In$_2$Se$_3$	VdWE on mica	Hexagonal (simple hexagonal, superlattice)	Semiconductor 1.26 eV (simple hexagonal) Metal (superlattice)	1 quintuple layer (QL), 1.30 nm 2 QL, 2.30 nm 3 QL, 3.30 nm	Several to hundreds of micrometers	Lin et al., 2013
	PVD on SiO$_2$/Si	α	Semiconductor 1.55 eV	Monolayer 1.00 nm	10.00 μm	Zhou et al., 2015
Bi$_2$Te$_3$	Catalyst-free vapor-solid (VS) growth on SiO$_2$/Si	Rhombohedral	Semiconductor	4 QL 4.08 nm	–	Kong et al., 2010
Bi$_2$Se$_3$				4 QL 3.96 nm		
Bi$_2$O$_2$Se	VdWE on mica	–	Semiconductor 0.80 eV	Monolayer 0.80 nm	>0.20 × 0.20 mm^2	Wu et al., 2017
Ga$_2$In$_4$S$_9$	Liquid-alloy-assisted CVD on mica	–	Semiconductor 2.76 eV	Bilayer 2.40 nm	Tens of micrometers	Wang et al., 2019

Table 2. Continued

inversely proportional to the migration energy barrier. It is necessary to choose substrates with small migration energy barrier to promote the migration of adatoms on the substrate. Mica without dangling bonds can facilitate rapid migration of adatoms and fast lateral crystal growth on it owing to small migration energy barrier of adatoms along the surface (Cheng et al., 2017). Besides, the thermal ionic motion in the molten glass causes the fluctuation of interatomic distance and weakens the interactions between adatoms

TMD Alloys	Component Ratio (x)	Preparation Detail	Structure Feature	Bandgap	Reference
$Mo_{1-x}W_xS_2$	x = 0–1.00	The reaction of MoO_{3-x} and WCl_6 with S by LPCVD	Monolayer Domain size 5.00 μm	Direct bandgaps by altering W proportion	Wang et al., 2016
		The reaction of MoO_3 and WO_3 with S	Monolayer Edge lengths from a few to dozens of micrometers	1.83–1.97 eV	Zhang et al., 2015
$MoS_{2x}Se_{2(1-x)}$	x = 0–0.68	The reaction of MoO_3 with S and Se using a simple moving source thermal evaporation method	Bilayer Thickness 1.65 nm	1.36–1.51 eV	Li et al., 2015
$MoS_{2(1-x)}Se_{2x}$	x = 0.41–1.00	The reaction of $MoSe_2$ and MoS_2 with Se	Monolayer Thickness 0.80 nm Domain size 10.00–20.00 μm	1.86–1.55 eV	Feng et al., 2015
$MoS_{2x}Se_{2(1-x)}$	x = 0–1.00	The reaction of MoO_3 with S and Se	Bilayer to trilayer Thickness 1.65–2.29 nm Domain size 80.00 μm	1.29–1.53 eV	Li et al., 2014
		The reaction of MoO_3 with S and Se	Monolayer Thickness 0.80 nm The edge lengths from a few to dozens of micrometers	1.55–1.97 eV	Zhang et al., 2015
$WS_{2(1-x)}Se_{2x}$	x = 0.18, 0.30 and 0.40	The reaction of WO_3 with S and Se	Monolayer Thickness 0.92 nm Domain size 26.00 μm	1.92–1.79 eV	Fu et al., 2015
$WS_{2x}Se_{2-2x}$	x = 0–1.00	The reaction of WS_2 and WSe_2	Monolayer Thickness 0.86 nm (x = 0.668)	1.98–1.65 eV	Duan et al., 2016

Table 3. Summary of 2DASCs of Alloyed TMDs

and growth substrates, lowing the migration barrier energy of adatoms to speed up the migration (Chen et al., 2017).

Nucleation and Growth of Crystals

The adatoms segregate on the substrate surface. When their concentration reaches a critical supersaturation level, nucleation happens (Kim et al., 2012). Based on the nucleation model of the vapor phase deposition, the nucleation probability is inversely proportional to the substrate temperature (Burton and Cabrera, 1949). Elevating the substrate temperature can reduce the nucleation rate and facilitate good regulation of the nuclei formation. Besides, precise control of the nucleation density is favorable to guide the further crystal growth. According to the equation (Kim et al., 2012),

$$N_S^3 \approx Pe^{\frac{G^*}{kT}}$$

where N_s is the saturation nucleation density, G^* is the nucleation barrier, and P is the partial pressure of the precursor; the nucleation density is inversely proportional to the temperature, so an increase in the temperature leads to a reduction of the nucleation density. After the nucleation, more reactants would diffuse to the edge of the nuclei and subsequently attach to the edge of the lattice for crystal growth. The Arrhenius equation is as follows:

$$k = Ae^{-\frac{E}{RT}}$$

where k is the reaction constant, R is the gas constant, T is the reaction temperature, E is the activation energy of decomposition, and A is the pre-exponential factor. It is concluded from this equation that increasing the reaction temperature can enhance the growth rate. Furthermore, the nucleation and growth of crystals can be modulated via introducing active elements. For instance, hydrogen can etch away unstable nuclei, terminate any broken or dangling bonds, and saturate the active edge of as-grown crystals,

Non-layered 2DASCs	Synthesis Method	Characteristics	Thickness	Domain Size	Reference
Mo_2C	The reaction of methane and Cu foil on Mo foil as the substrate	Superconductor	6.70 nm	>100.00 μm	Xu et al., 2015
	CVD on graphene with a Mo-Cu alloy	Superconductor	8.32 nm	100.00 μm	Geng et al., 2017
Ge	Halide-assisted self-limited CVD growth on SiO_2/Si	Semiconductor 0.67 eV	8.50 nm	–	Hu et al., 2018
GaN	Surface-confined nitridation reaction on Ga	Semiconductor 3.76 eV	4.10 nm	50.00 μm	Chen et al., 2018
CuI	PVD on SiO_2/Si	Semiconductor	1.00 nm	Several micrometers	Yao et al., 2018
Mo_2GaC	Confined chemical reaction on Ga_2O_3	Superconductor	2.20 nm	10.00 μm	Zeng et al., 2019
PbS	VdWE on graphite	Semiconductor 0.40 eV	5.00–35.00 nm	1.80–3.00 μm	Wen et al., 2016
CdS	VdWE on mica	Semiconductor	6.00 nm	44.00 μm	Jin et al., 2018
CdTe	VdWE on mica	Semiconductor 1.55 eV	5.00–15.00 nm	5.00–11.00 μm	Cheng et al., 2017
Cr_2S_3	VdWE on mica	Semiconductor	One unit cell thick 1.78 nm	200.00 μm	Chu et al., 2019
	Confined-space CVD on mica		2.50 nm	40.00 μm	Zhou et al., 2019
CrSe	VdWE on mica	Ferromagnetic Transition temperature close to 280 K	2.50 nm	150.00 μm	Zhang et al., 2019
CoSe	CVD on SiO_2/Si	Metal	3.70 nm	40.00 μm	Ma et al., 2019
CuI	PVD on SiO_2/Si	Semiconductor	1.00 nm	Several micrometers	Yao et al., 2018

Table 4. Summary of Non-layered 2DASCs

preventing further growth (Zhang et al., 2019). In addition, hydrogen saturation can stabilize graphene edges by reducing the detachment rates of carbon-containing species (Li et al., 2017). Oxygen can suppress the nucleation by eliminating unstable nuclei (Chen et al., 2015).

Furthermore, the growth of 2DASCs is influenced by substrates. 2DASCs grown on c-plane sapphire with specific lattice orientation and surface terraces show a specific orientation (Suenaga et al., 2018; Ji et al., 2018; Dumcenco et al., 2015). Mica with an atomically smooth surface is perfect for van der Waals epitaxy (vdWE). The lattice mismatch is significantly reduced owing to weak vdW interactions between the grown crystals and the substrate. Monolayer MX_2 (M = Re, W; X = Se, S) crystals can be grown on Au with low solubility and high catalytic activity (Gao et al., 2015, 2017; Jiang et al., 2018). Self-limiting growth of 2DASCs can be realized by utilizing the phase transition of liquid metals (Zeng and Fu, 2018). In addition, when the adhesive force of substrate surface is stronger than the cohesive force of adatom, layer grows. On the contrary, island growth occurs. Therefore, when selecting a suitable substrate for the growth of 2DASCs, the adhesive force of substrate surface and solubility should be taken into consideration.

Carrier gas also significantly influences the growth of 2DASCs (Li et al., 2018; Zhang et al., 2017) CVD growth of 2DASCs is more dictated by kinetics rather than thermodynamics with high flow rate. It ensures the attachment of precursors to the most active site at the edge of crystals, the formation of a good deal of nuclei, and the growth of thin, small crystals. In contrast, a low flow rate decreases the mass transfer and then slows down the nucleation and growth rate. As a result, thick crystals with large domain size are grown (Li et al., 2018).

PRECISE SYNTHESIS OF LAYERED 2DASCS

Layer Number Tuning

A large number of layered 2DASCs exhibit layer-dependent properties due to vdW interlayer coupling. For the majority of TMDs, their band gap decreases with increasing layer number. For example, semiconducting MoS_2, $MoSe_2$, WS_2, and WSe_2 show a transition from indirect to direct bandgap when their thickness decreases from bulk to monolayer (Mak et al., 2010). Great efforts have been devoted to controlling the layer number of layered 2DASCs down to monolayer and bilayer.

To grow monolayer graphene single crystals, it is necessary to efficiently suppress the carbon precipitation and prevent the inhomogeneous crystal growth via rationally designing growth substrates (Dai et al., 2011; Chen et al., 2015; Wang et al., 2013). The carbon solubility in the substrate influences the dissolution of active species (Wu et al., 2014). For high-carbon-soluble metals, such as Ni, massive species would segregate from bulk metals and precipitate on the surface during cooling, leading to nonuniform multilayer graphene (Edwards and Coleman, 2013). For those with low carbon solubility such as Cu, the active species for the nucleation and growth of graphene are dominated by the surface diffusion of the decomposed carbon sources, primarily leading to single-layer graphene (Zhang et al., 2014; Li et al., 2009). Besides, a cooling rate significantly affects the segregation of carbon species from the substrate (Yu et al., 2008) and monolayer graphene single crystals can be obtained with a low cooling rate (Wang et al., 2012). Monolayer graphene single crystals can also be synthesized by raising the H_2/CH_4 molar ratio (Wang et al., 2012; Zhou et al., 2013), as a continuous supply of the active carbon species from pyrolysis of CH_4 can sustain the graphene growth, and H_2 decomposes to form active atomic hydrogen, acting as an etching agent to graphene. The growth of hexagonal boron nitride (h-BN) on Cu is mainly surface mediated (Kim et al., 2012; Tay et al., 2014). In contrast, the growth on Ni is neither surface limited nor dominated by segregation and precipitation of B and N, but rather depends on the surface chemistry of Ni–B and Ni–N (Ismach et al., 2012). Monolayer h-BN single crystals were grown on Cu–Ni alloy with 10–20 atom % Ni on the basis of the surface-mediated mechanism on Cu (Lu et al., 2015).

Monolayer TMDs become principal building blocks in various optoelectronic devices owing to their direct bandgaps (Mak et al., 2010; Splendiani et al., 2010). For the growth of monolayer TMDs, it is necessary to avoid segregation and precipitation processes for multilayer growth. For instance, Au can decrease the barrier energies for the sulfurization of WO_3 (Figure 1A), allowing a very low concentration of WO_3 and S to grow monolayer WS_2. Besides, owing to the low solubility of W in Au, the segregation and precipitation processes for growing multilayer crystal would not happen. Therefore, monolayer WS_2 single crystals were grown on Au (Figure 1B), following a self-limited surface-catalytic process (Gao et al., 2015). The single-crystal nature of this large WS_2 domain is confirmed by the nearly identical crystallographic orientations in Figure 1C. Similarly, monolayer $ReSe_2$ single crystals were grown on Au (Jiang et al., 2018). Additionally, liquid soda-lime glass was employed as the substrate to trap the overflowing Mo source and suppress the precipitation, thus preventing the multilayer growth of MoS_2 (Figure 1D). The optical image of triangle-shaped monolayer MoS_2 single crystals is illustrated in Figure 1E (Ju et al., 2017). The intrinsic single-crystal nature of MoS_2 is verified by the only one set of diffraction spots of selected area electron diffraction (SAED) pattern in Figure 1F. In addition, the vertical growth of TMDs is suppressed via occupying active sites of the surface. Cu is attached at the surface of WSe_2, making W atoms only adsorb on the edge of monolayer crystals (Figure 1G) (Liu et al., 2016). Consequently, the growth process was dominated by size enlargement rather than layer accumulation, obtaining monolayer WSe_2 (Figure 1H). One set of diffraction pattern demonstrates the single crystallinity nature of the WSe_2 crystal (Figure 1I). The growth of monolayer TMDs can also be enabled by promoting the lateral growth. The small migration energy barrier of Hf and S atoms on mica causes a high migration rate along the substrate, leading to fast lateral growth of monolayer HfS_2 single crystals via vdWE (Fu et al., 2017). In summary, for the growth of monolayer layered 2DASCs, one effective strategy is to prevent the segregation and precipitation processes for the multilayer growth. Another strategy is to avoid the vertical growth as well as promote the lateral growth.

Bilayer single crystals are important basic structures for the research of atomic interactions between single layers. Bilayer graphene (BLG) is a semiconductor with continuously tunable electronic bandgap and electrical properties by a vertical electric field (Ohta et al., 2006; Castro et al., 2007; Zhang et al., 2009). It is not readily achievable for BLG on Cu, as the catalytic behavior of Cu is passivated by monolayer graphene formed on the substrate and further decomposition of the carbon sources for the growth of multilayer graphene is prevented. A high H_2/CH_4 ratio was applied in a low-pressure CVD (LPCVD) process to
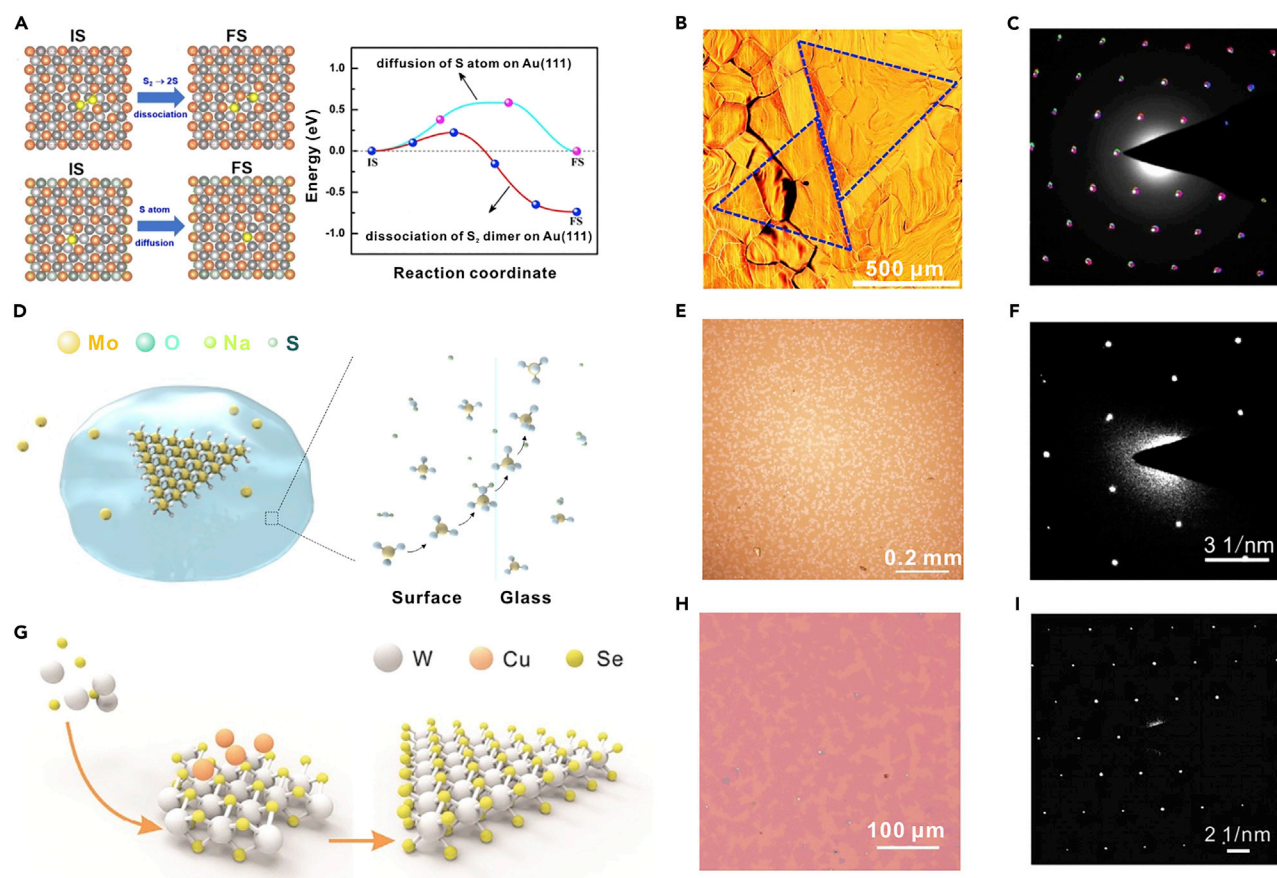
Figure 1. Synthesis of Monolayer 2DASCs

(A) Schematic of the initial state (IS) and the final state (FS) for the dissociation of S_2 into two S atoms, S atom diffusion on Au (111) surface, and the calculated minimum energy paths for these two processes.

(B) Optical image of monolayer single-crystal WS_2 domains on Au foil.

(C) Superimposed image of 12 SAED patterns taken from different parts of the same WS_2 domain. Reprinted with permission from Gao et al., 2015. Copyright 2015, Nature Publishing Group.

(D) Schematic illustration of the growth process of monolayer MoS_2 single crystals.

(E) Optical image of monolayer MoS_2 single crystals.

(F) SAED pattern of the MoS_2 crystal. Reprinted with permission from Ju et al., 2017. Copyright 2017, American Chemical Society.

(G) Schematic diagram of the Cu-assisted self-limited growth process of monolayer WSe_2 single crystals.

(H) Optical image of monolayer WSe_2 single crystals.

(I) SAED pattern of the WSe_2 crystal. Reprinted with permission from Liu et al., 2016. Copyright 2016, John Wiley & Sons, Inc.

partially expose the Cu surface and break the self-limiting effect of graphene growth on Cu, thus enabling the growth of BLG (Liu et al., 2012). There are two different stacking orders of layers in BLG. AA stacking refers to the twist angle of 0° and AB stacking refers to the twist angle of 30°. Importantly, high growth temperature and low pressure are favorable for the diffusion of the active carbon species to the lowest energy state, thus achieving AB-stacked graphene. Additionally, it is difficult for carbon species to diffuse across the edge of the first layer to participate in the growth of the second layer, as most of them may be captured by the first layer. Increasing the CH_4/H_2 ratio can elevate the supersaturation of carbon precursors and increase the possibility for the active species to cross the edge of the first layer, thus facilitating the growth of AB-stacked BLG single crystals (Zhou et al., 2013). Furthermore, an oxygen-rich Cu pocket was utilized in growing AB-stacked BLG single crystals, as shown in Figure 2B. Oxygen is required for dehydrogenation of CH_x so that carbon can diffuse through the Cu foil for the second layer growth on the exterior surface. In other words, oxygen activates hydrocarbon molecule dissociation and opens up the kinetic pathway for BLG growth. The first-layer graphene growth followed the surface-mediated mechanism, and the second layer was produced by the diffused carbon atoms from the interior (Figure 2A) (Hao et al., 2016).
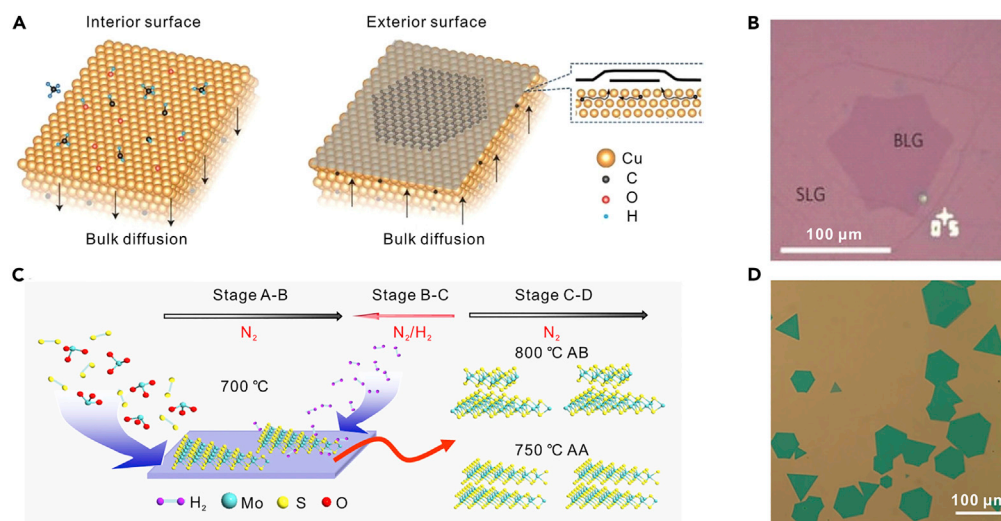
Figure 2. Synthesis of Bilayer 2DASCs

(A) Illustration of dynamic growing processes of the bilayer graphene from the interior to exterior surfaces of the Cu pocket.

(B) Optical image of the bilayer graphene domain. Reprinted with permission from Hao et al., 2016. Copyright 2016, Nature Publishing Group.

(C) Schematic illustration of the reverse-flow chemical vapor epitaxy process for bilayer MoS_2 single crystals.

(D) Optical image of the bilayer MoS_2 single crystals. Reprinted with permission from Zhang et al., 2019. Copyright 2019, Nature Publishing Group.

Bilayer TMDs crystals are attractive for applications in thin-film transistors, logic devices, and sensors owing to their high density of states, carrier mobility, and stability at room temperature. To grow bilayer TMDs, it is essential to ensure the second layer growth from the nucleation centers on the first layer and hinder further multilayer growth by avoiding new nucleation centers. The reverse carrier gas flow N_2/H_2 from the substrate to the source can prevent unintended precursor supply to suppress new nucleation centers on the first layer of MoS_2 crystal (Figure 2C) (Zhang et al., 2019). Additionally, H_2 can prevent the lateral growth by saturating the dangling bonds of the first layer and slightly etch away nucleation sites on the substrate. Therefore, the source vapor can migrate on the substrate surface and reach the first-layer surface. As a result, the second layer was grown from the activated nucleation centers of the first one. Bilayer MoS_2 with triangle and hexagon shapes can be observed on the substrate (Figure 2D). Furthermore, the AA (twist angle of 0°) and AB (twist angle of 60°) stacking orders of the bilayer crystals are decided by their stability and thermodynamic energy (Zhang et al., 2019). To sum up, several effective methods can be utilized to synthesize bilayer 2DASCs. The possibility for the active species to cross the edge of the first layer should be increased. In addition, new nucleation centers should be avoided to ensure the second-layer growth from existing nucleation centers on the first layer.

Besides, TMDs single crystals with tunable layer numbers can be synthesized via controlling the growth temperature (Zhao et al., 2018). Low substrate temperature makes the growth kinetically controlled and accelerates the nucleation rate. Therefore, the source atoms were quickly added to the fastest growth front dominated by edge energetics, obtaining thin crystals. In comparison, at high substrate temperature, the growth is more thermodynamically controlled, leading to a low nucleation rate to produce thick crystals (Figure 3A). Atomic force microscopy (AFM) images of the as-grown $NiTe_2$ crystals at different temperatures confirm a systematic thickness evolution from monolayer to seven layers. The SAED patterns in the insets of Figure 3B show a single set of diffraction spots, suggesting the single-crystal nature of the as-grown sample. Similarly, $PtTe_2$ single crystals with tunable layer numbers were synthesized (Ma et al., 2018). Besides, layer-controlled growth of TMDs single crystals can be achieved by lowing the transport rate. Monolayer MoS_2 crystals were grown by using I_2 as a transport agent in the CVT process (Hu et al., 2017). The concentration of Mo source in the gas phase was reduced, and the temperature gradient was enlarged to slow down the transport process and dramatically decrease the growth rate. Similarly, $PtSe_2$ crystals with controlled layer numbers were obtained with KCl as a transport agent in CVT process, as
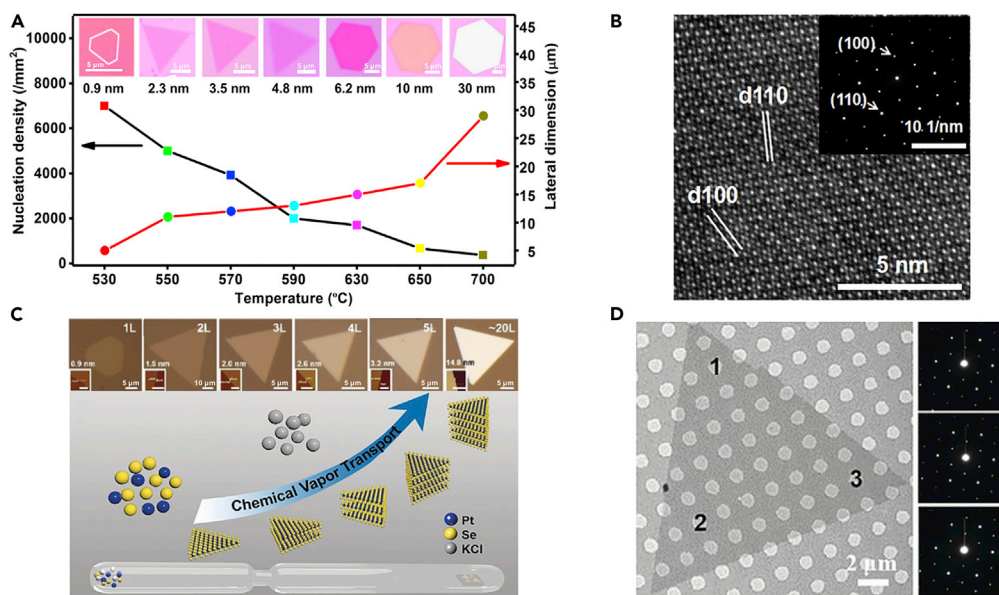
Figure 3. Synthesis of 2DASCs with Tunable Layer Numbers

(A) Evolution of the thickness (inset) of $NiTe_2$ single crystals obtained at different temperatures.

(B) HRTEM image of the $NiTe_2$ crystals (inset shows the corresponding SAED pattern). Reprinted with permission from Zhao et al., 2018. Copyright 2018, American Chemical Society.

(C) Illustration of the layer-controlled synthesis of $PtSe_2$ single crystals by CVT method.

(D) Optical image of 2D single-crystal $PtSe_2$ domains. Reprinted with permission from Hu et al., 2019. Copyright 2019, John Wiley & Sons, Inc.

illustrated in Figure 3C (Hu et al., 2019). Figure 3D shows the triangular-shaped $PtSe_2$ crystals, and the SAED patterns confirm their single-crystalline nature. In short, the layer number of 2DASCs can be precisely adjusted by controlling the growth temperature or modulating the transport rate of the source.

Phase Selecting

Variations in the atomic arrangement or symmetry of 2D TMDs could induce the variety in their properties. TMDs exhibit different electronic characters, including metallic, semimetallic, semiconducting, and super-conducting behavior, which are highly dependent on their phases. Precise phase control of 2D TMDs is a vital issue in future research and applications. Trigonal prismatic (1H) phase and octahedral (1T) phase of TMDs are based on different combinations of metal and chalcogen atoms. In addition, there are two different stacking ways for 1H-TMDs, namely, hexagonal symmetry (2H phase) and rhombohedral symmetry (3R phase) (Voiry et al., 2015). Owing to different filling electrons of d orbitals of transition metals, 1T phase would evolve into two variants, including the distorted octahedral (1T′) and orthorhombic (T_d, under low temperature or high pressure) phases. Generally, 2D TMDs prefer to exist in the form of the most thermodynamically stable phase, whereas 2D metastable-phase ones are difficult to obtain owing to their higher formation energy. The formation energy barrier of metastable-phase TMDs should be overcome to synthesize metastable-phase crystals. Herein, several strategies to achieve this goal are summarized.

Pure phase synthesis can be achieved via slightly changing the growth temperature (T_G) owing to small differences in ground-state energy between several phases. For instance, the energy difference per formula unit between $2H-MoTe_2$ and $1T′-MoTe_2$ is ~0.03 eV (Li et al., 2016). Therefore, it is necessary to accurately control T_G. As shown in Figure 4A, few-layer $1T′-MoTe_2$ crystals were grown at T_G = 710°C. In contrast, at T_G = 670°C, few-layer $2H-MoTe_2$ ones were obtained (Sung et al., 2017). The scanning tunneling microscope (STM) images display different atomic structures of 2H- and $1T′-MoTe_2$, respectively. The STM image in Figure 4B shows that the layers of $1T′-MoTe_2$ are periodically corrugated along the a axis and the Mo atoms occupy deformed Te octahedra. In contrast, the sandwiches Te-Mo-Te, which are built of trigonal prisms, are perpendicular to the hexagonal c axis (Figure 4C).
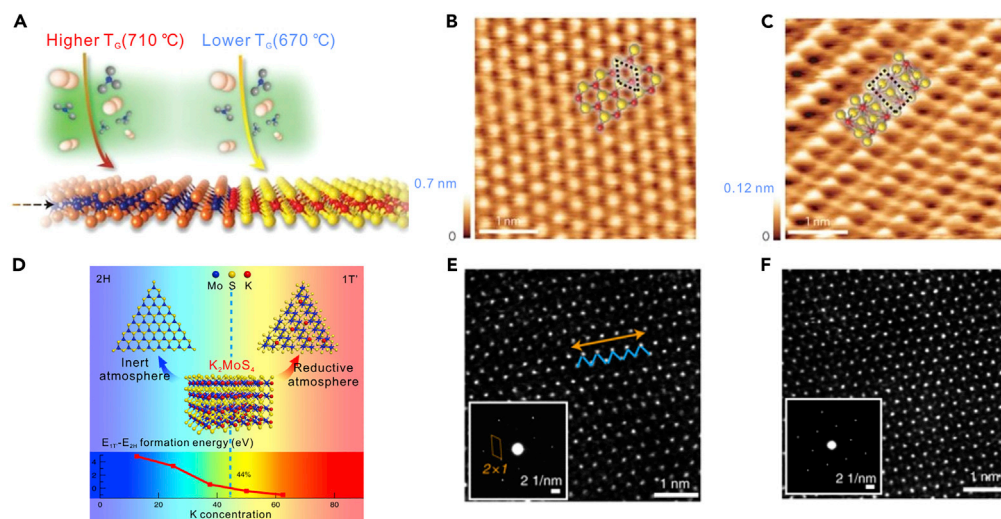
Figure 4. Pure Phase Synthesis of 2D TMDs Single Crystals

(A) Illustration of phase-selective synthesis of 2H- or 1T'-MoTe$_2$ through temperature control.

(B and C) STM topography images of 2H-MoTe$_2$ and 1T'-MoTe$_2$, respectively. Reprinted with permission from Sung et al., 2017. Copyright 2017, Nature Publishing Group.

(D) Schematic illustration of the synthesis of 2H- or 1T'-MoS$_2$ by controlling the formation energy. The inset plots below display the difference in the formation energy between 1T'- and 2H-K$_x$MoS$_2$ as a function of K concentration.

(E) Atomically resolved filtered STEM images of 1T'-MoS$_2$ flakes. Insets of E, SAED patterns of 1T'-MoS$_2$ single-crystal flakes.

(F) Atomically resolved filtered STEM images of 2H-MoS$_2$ flakes. Insets of F, SAED patterns of 2H-MoS$_2$ single crystals. Reprinted with permission from Liu et al., 2018. Copyright 2018, Nature Publishing Group.

Pure phase synthesis can also be realized by decreasing the formation energy of metastable-phase intermediates. For phase control of MoS$_2$, the relative stabilities of two intermediates, namely, 1T'- and 2H-K$_x$MoS$_2$ can be changed by adjusting the K concentration under a reductive and inert atmosphere, respectively (Liu et al., 2018). When the K concentration reaches over 44%, 1T'-K$_x$MoS$_2$ is more stable than 2H-K$_x$MoS$_2$ (Figure 4D). As a result, monolayer 1T'-MoS$_2$ crystals were obtained in H$_2$ atmosphere, which is verified by zigzag chains with a shortest Mo–Mo distance (Figure 4E) and the superstructure in the SAED patterns (inset of Figure 4E). Monolayer 2H-MoS$_2$ crystals were also grown in Ar atmosphere, as confirmed by the atomically resolved high-angle annular dark-field scanning transmission electron microscopy (HAADF-STEM) images in Figure 4F and the SAED patterns (inset of Figure 4F). Moreover, the formation energy of 1T'-MoTe$_2$ can be reduced by iodine (Zhang et al., 2017). It is theoretically calculated that the iodine-adsorbed 1T'-MoTe$_2$ is more stable than iodine-adsorbed 2H-MoTe$_2$. The 1T' phase can also be stabilized with the enlarged bond length of Mo–Te by I$_2$, lowering the energy of the 1T' phase and facilitating its synthesis. Additionally, monolayer and few-layer 1T'-MoTe$_2$ and 1T'-WTe$_2$ crystals have been grown with KCl or NaCl, respectively (Chen et al., 2017). Volatile MoO$_2$Cl$_2$ (WO$_2$Cl$_2$) and MoOCl$_4$ (WO$_2$Cl$_2$) were produced during the reaction of the halides with Mo (W) precursor, and the reaction with Te was accelerated. In summary, to synthesize metastable-phase 2D TMDs, it is essential to differentiate the relatively small difference in the ground-state energy between metastable and stable phase via accurately tuning temperature or decreasing the formation energy of metastable-phase intermediates.

Chemical Composition Controlling

Chemical composition controlling can tune the properties of 2DASCs to supplement their intrinsic properties. Chemical composition tuning includes atomic doping and alloying. For heteroatom doping, the dopant atoms are incorporated into the crystal lattice of 2D TMDs via either replacing the lattice atoms or squeezing into the interstitial sites of the lattice. In principle, the doping concentration should be lower than a certain percentage to ensure that the intrinsic crystal structure of the host materials is not altered by the dopants. The band structure of the doped 2DASCs could be modulated by accurately adjusting dopant type and doping level. It is important to choose an appropriate precursor to realize ordered doping (Cui et al., 2017). In contrast, in alloyed 2DASCs, one of the elements is partially substituted by another element,
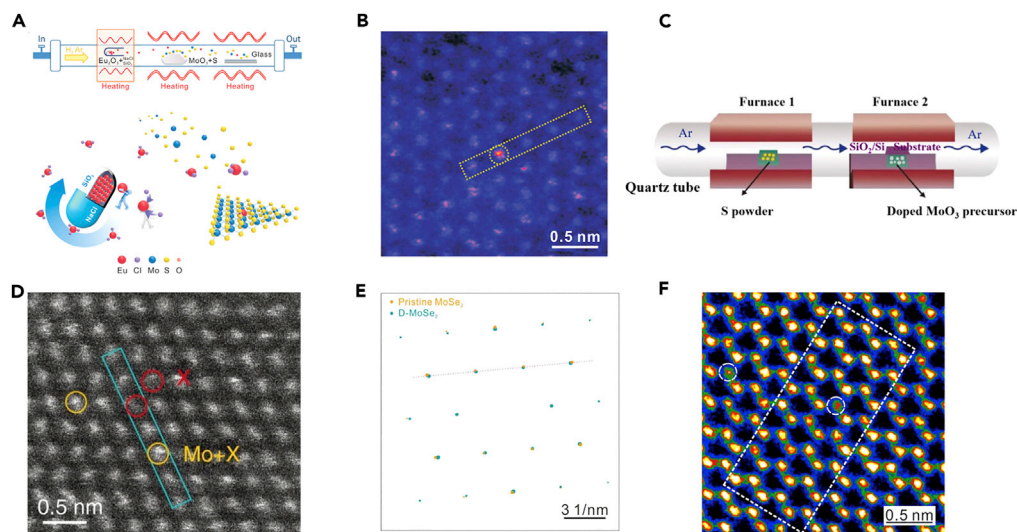
Figure 5. Doping of 2D TMDs Single Crystals

(A) Illustration of the growth of monolayer MoS_2 single crystals doped with Eu.

(B) HAADF-STEM atomic image of the monolayer MoS_2 single crystals doped with Eu. Reprinted with permission from Xu et al., 2018. Copyright 2018, John Wiley & Sons, Inc.

(C) Schematic of the CVD process of MoS_2 monolayers doped with Co and Cr.

(D) HAADF-STEM image of (Co, Cr)-MoS_2 monolayer single crystal. Reprinted with permission from Duan et al., 2019. Copyright 2019, Nature Publishing Group.

(E) SAED patterns of the pristine $MoSe_2$ and D-$MoSe_2$ single crystals.

(F) HAADF-STEM image of the monolayer donor-doped $MoSe_2$ single crystal. Reprinted with permission from Liu et al., 2019. Copyright 2019, Elsevier.

with the crystal structures remaining homogeneous. Compared with that in heteroatom doping, the percentage of substitution in 2D alloyed TMDs can be flexibly tunable.

Atomic doping of 2D TMDs crystals can be realized via slow and steady precursor supply during the CVD growth. Monolayer MoS_2 crystals doped by rare-earth element were grown via a matrix-assisted sustained-release CVD method, as illustrated in Figure 5A (Xu et al., 2018). During the CVD process, Eu_2O_3 was transformed into volatile $EuCl_3$ with the promotion of NaCl. On the other hand, silicate was produced to continuously release Eu. A sustainable supply of Eu contributes to the doping of MoS_2 crystals, regardless of the significant difference between the covalent radius of Eu and Mo. The HAADF-STEM image in Figure 5B confirms the existence of Eu in the crystal. Besides, monolayer MoS_2 crystals can be doped by utilizing (Co, Cr)-co-doped MoO_3 and S as precursors via CVD method, as displayed in Figure 5C (Duan et al., 2019). This method contributes to the homogeneous distribution of Co, Cr, and MoO_3 at the molecular level. Co and Cr atoms entering the lattice of MoO_3 are likely to adopt a similar coordination structure to that of Mo atoms. Consequently, (Co, Cr)-MoS_2 crystals can be obtained without the precipitation of Co and Cr from the MoS_2 monolayers. Figure 5D shows the location of Cr and Co atoms within the crystal, confirming the doping of Co and Cr in it. Furthermore, a metal foil such as Fe, Cu, or Ni was utilized as precursor for growing monolayer donor-doped $MoSe_2$ (D-$MoSe_2$) crystals (Liu et al., 2019). As displayed in Figure 5E, different repeating intervals between the SAED patterns of the doped and pristine single crystal reveal distinct lattice structures. The HAADF-STEM image in Figure 5F shows the doping site of monolayer D-$MoSe_2$ crystal at the atomic scale, and the precise positions are marked by circles. In brief, doping of 2DASCs can be realized via the continuous and steady supply of precursor containing the doping elements during the CVD process.

Alloying is useful in adjusting electronic structures and lattice parameters of 2D TMDs crystals (Xie, 2015). The valence band position in TMDs is generally contributed by the d-orbital of the metal and the valence electron of chalcogenides (Chhowalla et al., 2013). In 2D alloyed TMDs, chalcogenide or metal is partially substituted by another one, modulating the bandgap and related optical properties. 2D alloyed TMDs crystals can be achieved with precursors containing the doping metal or chalcogenides via CVD method.
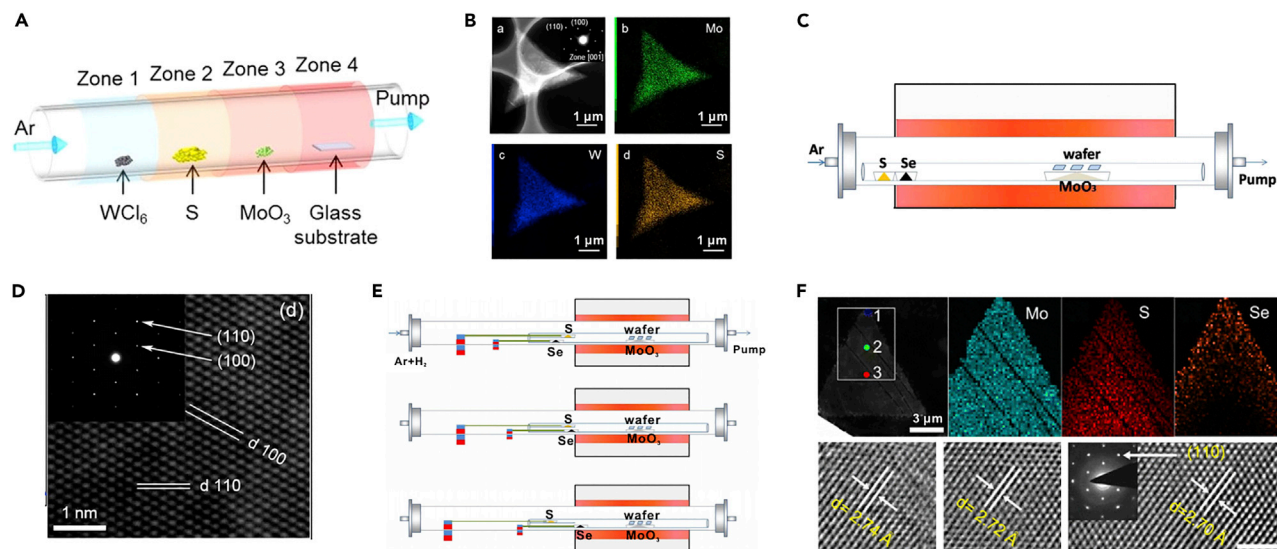
Figure 6. Alloying of 2D TMDs Single Crystals

(A) Schematic of the setup for the growth of $Mo_{1-x}W_xS_2$ single crystals.

(B) HAADF-STEM image and EDS element mappings of the $Mo_{1-x}W_xS_2$ crystals. The SAED pattern (the inset of B) reveals the single-crystal nature of the crystal. Reprinted with permission from Wang et al., 2016. Copyright 2016, Nature Publishing Group.

(C) Schematic of the setup for the growth of $MoS_{2x}Se_{2(1-x)}$ single crystals.

(D) HRTEM image and its SAED pattern (inset) of single-crystal $MoS_{2x}Se_{2(1-x)}$ domains. Reprinted with permission from Li et al., 2014. Copyright 2014, American Chemical Society.

(E) Schematic of the setup for the lateral growth of composition graded atomic layer $MoS_{2(1-x)}Se_{2x}$ nanosheets.

(F) Typical TEM image, 2D elemental mapping, and HRTEM images of the obtained 2D $MoS_{2(1-x)}Se_{2x}$ single crystals with lateral graded composition. Reprinted with permission from Li et al., 2015. Copyright 2015, American Chemical Society.

So far, two types of 2D TMD alloys, i.e., $M_xM'_{1-x}X_2$ and $MX_xX'_{2(1-x)}$, have been prepared, as summarized in Table 3.

In the $M_xM'_{1-x}X_2$-type alloy, one of the transition metal elements is partially substituted by another one. For example, volatile WCl_6 makes the growth temperature of WS_2 close to that of MoS_2. Therefore, MoO_3 and WCl_6 can be simultaneously utilized as sources to grow monolayer $Mo_{1-x}W_xS_2$ crystals by LPCVD (Figure 6A) and the Mo/W ratio can be tailored by tuning the MoO_3 and WCl_6 supplies (Wang et al., 2016). As illustrated in Figure 6B, the energy dispersive X-ray spectroscopy (EDS) mappings reveal the homogeneous distributions of Mo, W, and S in the crystal, and the SAED pattern (inset of Figure 6B) confirms that the as-grown $Mo_{1-x}W_xS_2$ are single crystals. Monolayer $Mo_{1-x}W_xS_2$ single crystals with fully tunable composition can also be grown by the sulfuration of MoO_3 and WO_3 in a CVD furnace (Zhang et al., 2015).

2D $MX_xX'_{2(1-x)}$-type single crystals with varying x values have been prepared via the CVD method as well. 2D $MoS_{2x}Se_{2(1-x)}$ crystals were grown by the sulfidation/selenylation of MoO_3 using one-step temperature gradient-assisted CVD route in Figure 6C (Li et al., 2014). High-resolution transmission electron microscopy (HRTEM) image in Figure 6D demonstrates the single-crystalline nature of the 2D structures. The SAED pattern in the inset of Figure 6D displays their hexagonal symmetry structures. Similar fabrication processes were also adopted to obtain monolayer $WS_{2(1-x)}Se_{2x}$ single crystals (Fu et al., 2015). Moreover, monolayer $WS_{2x}Se_{2(1-x)}$ crystals with fully tunable compositions can also be obtained by using WS_2 and WSe_2 as precursors (Duan et al., 2016). The S/Se ratios in the as-grown crystals could be tuned by controlling the evaporation temperature of WS_2 and WSe_2. Similarly, the growth of monolayer $MoS_{2(1-x)}Se_{2x}$ (x = 0.41–1.00) alloys can be realized with MoS_2 and $MoSe_2$ as precursors (Feng et al., 2015).

In addition to the fact that the chemical compositions vary among 2D single crystals of different alloyed TMDs, the atomic ratio in a specific 2D alloyed crystal can be tuned as well. Monolayer $MoS_{2(1-x)}Se_{2x}$ crystals were grown, and the composition was varied from the center to the edge of the crystal via a moving

source thermal evaporation method (Figure 6E) (Li et al., 2015). The heating temperature of Se was gradually increased, followed by the decrease in the maintaining temperature of S. Thus, the lateral composition-graded alloy could be synthesized by controlling the ratio of vaporized precursors. Figure 6F further shows the 2D elemental mapping for Mo, S, and Se, respectively, in a selected region of the crystal, suggesting uniform distribution of Mo across the whole area, with the main location of S at the center and dominant distribution of Se at the edge region. The elemental analyses further demonstrate that these alloys are laterally graded in composition. The SAED pattern of the crystal in the inset of Figure 6F shows a clearly defined single set of diffraction spots, further demonstrating its single-crystalline nature. The position-dependent photoluminescence (PL) spectrum of the crystals verified a lateral composition variation. In summary, for obtaining 2D alloyed TMDs single crystals with different chemical compositions, it is necessary to tune the ratio of several precursors by controlling their evaporation, ensure steady and continuous precursor supply, and control the deposition of products during the growth.

PRECISE SYNTHESIS OF NON-LAYERED 2DASCS

For non-layered 2DASCs, their surfaces are filled with dangling bonds, rendering them highly chemically active and enhancing their capability of catalysis, sensing, and carriers transfer. Typical non-layered materials, III–VA group semiconductors, have both high carrier mobilities and direct bandgaps. However, it is challenging to achieve ultrathin non-layered 2DASCs owing to the naturally intrinsic covalent bonds. Several efforts have been devoted to achieving this goal.

Non-layered 2DASCs can be grown via reducing the precursor supply to confine the vertical crystal growth. The growth of 2D GaN crystals was limited on the surface of Ga–W solid solution owing to the stronger nitridation ability of W than Ga, as illustrated in Figure 7A. Therefore, the thickness of the crystal was well controlled down to 4.1 nm (Figure 7B) (Chen et al., 2018). The SAED pattern in Figure 7C indicates the single-crystal nature of the GaN domain. Besides, non-layered 2DASCs can be achieved by confining the isotropic growth along with three-dimensional directions. Ultrathin single-crystal Ge flakes were grown as Cl prefers to adsorb on the (111) plane of the Ge surface (Figure 7D). The AFM image in Figure 7E shows that the thickness of the Ge flake is as thin as 8.5 nm (Hu et al., 2018). Figure 7F illustrates the SAED pattern, and the sharp spots also identify the single-crystalline structure and the preferential growth of (111) planes. Non-layered 2DASCs can be synthesized by rationally designing 2D templates as well. Recently, confined chemical reaction of ultrathin Mo_2GaC single crystals was realized by designing a precise molecular scaffold, an ultrathin Ga_2O_3 layer (Zeng et al., 2019), which is initially one-unit-cell thick (Figure 7G). AFM image in Figure 7H confirms that the thickness of the crystal is around 2.2 nm, consistent with the value of the Mo_2GaC unit cell. Figure 7I shows the SAED pattern of the crystal. Besides, the energy barrier of lateral growth along the substrate can also be decreased to obtain non-layered 2DASCs. For instance, the exposed (001) face of mica exhibits chemical inertness and atomically smooth surface. Consequently, the migration energy barrier of adatoms along the surface is small, facilitating rapid migration of adatoms and fast lateral growth of ultrathin Cr_2S_3, CdTe, and CrSe crystals via vdWE (Cheng et al., 2017; Chu et al., 2019; Zhang et al., 2019). Overall, it is of great significance to suppress the vertical crystal growth, prevent the isotropic crystal growth in three dimensions, provide 2D templates, or facilitate the lateral growth along the substrate to achieve non-layered 2DASCs.

CONCLUSION AND OUTLOOK

In summary, this review provides insights into the growth process and growth mechanism of 2DASCs in vapor phase. Then recent achievements in the precise synthesis of layered 2DASCs are presented from three aspects, namely, layer number tuning, phase selecting, and chemical composition controlling. Furthermore, the synthesis of ultrathin non-layered 2DASCs is discussed in details. Herein, we outline several possible directions to further promote the developments in the precise synthesis of 2DASCs for practical applications.

Although some advances have been made in controlling the layer number of 2DASCs, it is still challenging to synthesize bilayer 2DASCs owing to uncontrollable nucleation centers on the second layer and further growth of multilayer. Bilayer graphene can be achieved by accurately controlling active carbon species supply during the segregation process for the growth of the second layer. For bilayer TMDs, new nucleation sites on the second layer should be prevented to avoid the growth of multilayer. Furthermore, research on the relationships between the layer number and the properties of 2DASCs is still hindered owing to the
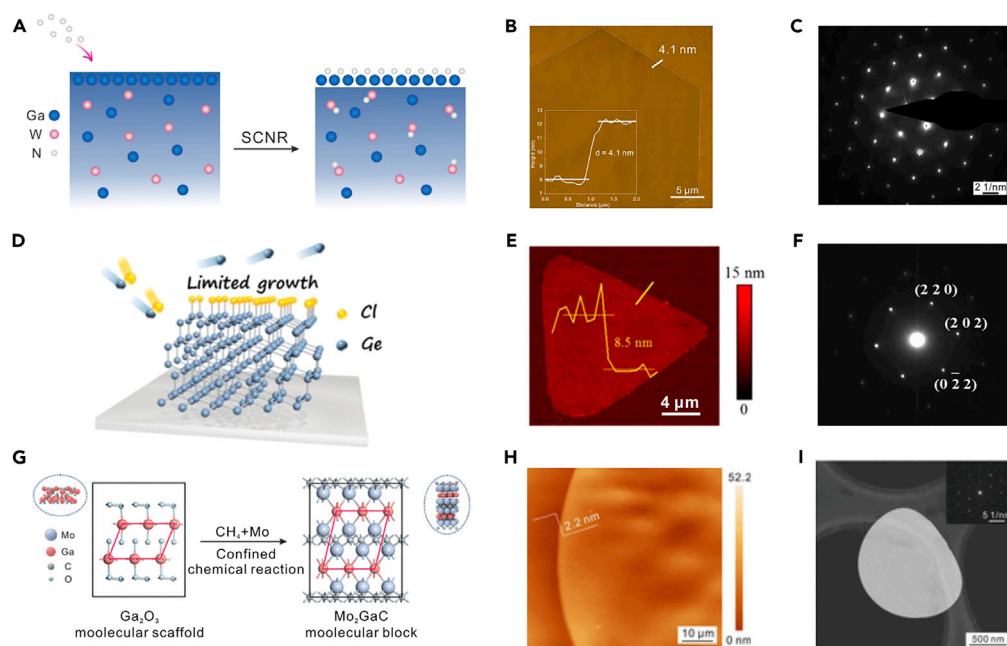
Figure 7. Synthesis of 2D Non-layered Single Crystals

(A) Schematic illustration of the growth of ultrathin GaN single crystals on liquid metals via a surface-confined nitridation reaction.

(B) AFM image of the 2D single crystal of GaN, and the inset is the thickness profile of the image.

(C) SAED pattern of the 2D GaN single crystal. Reprinted with permission from Chen et al., 2018. Copyright 2018, American Chemical Society.

(D) Schematic illustrating the growth of thin Ge single-crystal flakes on liquid metals via a halide-induced self-limited growth.

(E) AFM image and thickness profile of an ultrathin single-crystal Ge flake.

(F) SAED pattern of the 2D Ge single crystal. Reprinted with permission from Hu et al., 2018. Copyright 2018, American Chemical Society.

(G) Schematic of the growth of 2D strong interlayer-bonding Mo_2GaC single crystals by designing a molecular scaffold.

(H) AFM image of the ultrathin single crystal of Mo_2GaC.

(I) A low-magnification HAADF-STEM image of a Mo_2GaC single crystal and SAED pattern of the crystal (inset). Reprinted with permission from Zeng et al., 2019. Copyright 2019, Chinese Chemical Society.

difficulty in growing crystals with tunable layer numbers (Zhao et al., 2018; Hu et al., 2019). It is imperative to develop a feasible and general method to achieve 2DASCs with continuously tunable layer numbers.

Controlling the phase of 2D TMDs through well-designed vapor growth methods will be the primary strategy in the future, as vapor growth methods such as CVD can achieve a good balance between considerable productivity and high quality of crystals. However, only the most stable phase can be obtained for many reported 2D TMDs. In this case, the proper design of precursors and growth promotors for synthesizing 2D metastable-phase TMDs is still required and urgent. Moreover, continuous efforts need to be made in pure phase synthesis of 2DASCs beyond TMDs to realize the potential of their properties (Ahn et al., 2015). Stability is also one of the most critical issues, as the metastable crystal structures might revert to the thermodynamically stable ones under the influence of elevated temperature or other external perturbations.

Besides, the distribution of heteroatoms in 2D heteroatom-doped TMDs crystals is usually random. It remains a challenge to accurately control the desired concentration and anchored position of dopant atoms in 2DASCs at the atomic level. Therefore, it is needed to ensure a steady supply and strictly tune the content of heteroatoms in precursors to realize doping with controllable concentration. However, owing to the same chemical environment for the element in a crystal lattice, fixed-point doping remains to be further explored, and novel approaches are urgently required. For alloying of 2DASCs, enriching the number of components would increase the freedom degree and provide more flexibility in tuning the bandgap.

Even though a great deal of efforts have been devoted to the vapor growth of 2D ternary alloyed TMDs crystals, it is still challenging to grow 2D quaternary alloyed TMDs ones without destroying their crystal structures (Susarla et al., 2017). Alloyed TMDs are required to have similar lattice/electronic structures and negative formation energy.

Ultrathin non-layered single crystals with thickness even below 2 nm have been successfully synthesized. Scaling down the thickness to one atom and obtaining uniform wafer-scale 2D non-layered crystals will be the next direction. For this purpose, new synthesis strategies are highly desired to obtain 2D non-layered crystals with larger domain size and unavailable ultrathin non-layered crystals.

In summary, regardless of the fact that we have witnessed significant progress in the past few years, precise vapor-phase synthesis of 2DASCs is still very challenging but is really essential for further research and practical applications.

AUTHOR CONTRIBUTIONS

Conceptualization, L.F.; Writing – Original Draft, S.Z. and L.W.; Writing – Review & Editing, L.F. and S.Z.; Supervision, L.F.

REFERENCES

Abild-Pedersen, F., Greeley, J., Studt, F., Rossmeisl, J., Munter, T.R., Moses, P.G., Skúlason, E., Bligaard, T., and Nørskov, J.K. (2007). Scaling properties of adsorption energies for hydrogen-containing molecules on transition-metal surfaces. Phy. Rev. Lett. 99, 016105.

Ahn, J.-H., Lee, M.-J., Heo, H., Sung, J.H., Kim, K., Hwang, H., and Jo, M.-H. (2015). Deterministic two-dimensional polymorphism growth of hexagonal n-type SnS_2 and orthorhombic p-type SnS crystals. Nano Lett. 15, 3703–3708.

Burton, W.K., and Cabrera, N. (1949). Crystal growth and surface structure. Part I. Discuss. Faraday Soc. 5, 33–39.

Caneva, S., Weatherup, R.S., Bayer, B.C., Brennan, B., Spencer, S.J., Mingard, K., Cabrero-Vilatela, A., Baehtz, C., Pollard, A.J., and Hofmann, S. (2015). Nucleation control for large, single crystalline domains of monolayer hexagonal boron nitride via Si-doped Fe catalysts. Nano Lett. 15, 1867–1875.

Castro, E.V., Novoselov, K.S., Morozov, S.V., Peres, N.M.R., dos Santos, J.M.B.L., Nilsson, J., Guinea, F., Geim, A.K., and Neto, A.H.C. (2007). Biased bilayer graphene: semiconductor with a gap tunable by the electric field effect. Phy. Rev. Lett. 99, 216802.

Chang, H.-C., Tu, C.-L., Lin, K.-I., Pu, J., Takenobu, T., Hsiao, C.-N., and Chen, C.-H. (2018). Synthesis of large-area InSe monolayers by chemical vapor deposition. Small 14, 1802351.

Chen, W., Zhao, J., Zhang, J., Gu, L., Yang, Z.Z., Li, X.M., Yu, H., Zhu, X.T., Yang, R., Shi, D.X., et al. (2015). Oxygen-assisted chemical vapor deposition growth of large single-crystal and high-quality monolayer MoS_2. J. Am. Chem. Soc. 137, 15632–15635.

Chen, L.F., Kong, Z.Z., Yue, S.L., Liu, J.X., Deng, J.W., Xiao, Y., Mendes, R.G., Rümmeli, M.H., Peng, L.M., and Fu, L. (2015). Growth of uniform monolayer graphene using iron-group metals via the formation of an antiperovskite layer. Chem. Mater. 27, 8230–8236.

Chen, J.Y., Zhao, X.X., Tan, S.J.R., Xu, H., Wu, B., Liu, B., Fu, D.Y., Fu, W., Geng, D.C., Liu, Y.P., et al. (2017). Chemical vapor deposition of large-size monolayer $MoSe_2$ crystals on molten glass. J. Am. Chem. Soc. 139, 1073–1076.

Chen, K., Chen, Z.F., Wan, X., Zheng, Z.B., Xie, F.Y., Chen, W.J., Gui, X.C., Chen, H.J., Xie, W.G., and Xu, J.B. (2017). A simple method for synthesis of high-quality millimeter-scale 1T′ transition-metal telluride and near-field nanooptical properties. Adv. Mater. 29, 1700704.

Chen, Y.X., Liu, K.L., Liu, J.X., Lv, T.R., Wei, B., Zhang, T., Zeng, M.Q., Wang, Z.C., and Fu, L. (2018). Growth of 2D GaN single crystals on liquid metals. J. Am. Chem. Soc. 140, 16392–16395.

Cheng, R.Q., Wen, Y., Yin, L., Wang, F.M., Wang, F., Liu, K.L., Shifa, T.A., Li, J., Jiang, C., Wang, Z.X., et al. (2017). Ultrathin single-crystalline CdTe nanosheets realized via van der Waals epitaxy. Adv. Mater. 29, 1703122.

Chhowalla, M., Shin, H.S., Eda, G., Li, L.-J., Loh, K.P., and Zhang, H. (2013). The chemistry of two-dimensional layered transition metal dichalcogenide nanosheets. Nat. Chem. 5, 263–275.

Chu, J.W., Zhang, Y., Wen, Y., Qiao, R.X., Wu, C.C., He, P., Yin, L., Cheng, R.Q., Wang, F., Wang, Z.X., et al. (2019). Sub-millimeter-scale growth of one-unit-cell-thick ferrimagnetic Cr_2S_3 nanosheets. Nano Lett. 19, 2154–2161.

Ciarrocchi, A., Avsar, A., Ovchinnikov, D., and Kis, A. (2018). Thickness-modulated metal-to-semiconductor transformation in a transition metal dichalcogenide. Nat. Commun. 9, 919.

Cui, P., Choi, J.-H., Zeng, C.G., Li, Z.Y., Yang, J.L., and Zhang, Z.Y. (2017). A kinetic pathway toward High-density ordered N doping of epitaxial graphene on Cu(111) using C_5NCl_5 precursors. J. Am. Chem. Soc. 139, 7196–7202.

Dai, B.Y., Fu, L., Zou, Z.Y., Wang, M., Xu, H.T., Wang, S., and Liu, Z.F. (2011). Rational design of a binary metal alloy for chemical vapour deposition growth of uniform single-layer graphene. Nat. Commun. 2, 522.

Duan, X.F., Wang, C., Fan, Z., Hao, G.L., Kou, L.Z., Halim, U., Li, H.L., Wu, X.P., Wang, Y.C., Jiang, J.H., et al. (2016). Synthesis of $WS_{2x}Se_{2-2x}$ alloy nanosheets with composition-tunable electronic properties. Nano Lett. 16, 264–269.

Duan, H.L., Guo, P., Wang, C., Tan, H., Hu, W., Yan, W.S., Ma, C., Cai, L., Song, L., Zhang, W.H., et al. (2019). Beating the exclusion rule against the coexistence of robust luminescence and ferromagnetism in chalcogenide monolayers. Nat. Commun. 10, 1584.

Dumcenco, D., Ovchinnikov, D., Marinov, K., Lazić, P., Gibertini, M., Marzari, N., Sanchez, O.L., Kung, Y.-C., Krasnozhon, D., Chen, M.-W., et al. (2015). Large-area epitaxial monolayer MoS_2. ACS Nano 9, 4611–4620.

Edwards, R.S., and Coleman, K.S. (2013). Graphene film growth on polycrystalline metals. Acc. Chem. Res. 46, 23–30.

Feng, Q.L., Mao, N.N., Wu, J.X., Xu, H., Wang, C.M., Zhang, J., and Xie, L.M. (2015). Growth of $MoS_{2(1-x)}Se_{2x}$ (x = 0.41–1.00) monolayer alloys

with controlled morphology by physical vapor deposition. ACS Nano 9, 7450–7455.

Fu, Q., Yang, L., Wang, W.H., Han, A.L., Huang, J., Du, P.W., Fan, Z.Y., Zhang, J.Y., and Xiang, B. (2015). Synthesis and enhanced electrochemical catalytic performance of monolayer $WS_{2(1-x)}Se_{2x}$ with a tunable band gap. Adv. Mater. 27, 4732–4738.

Fu, L., Wang, F., Wu, B., Wu, N., Huang, W., Wang, H.L., Jin, C.H., Zhuang, L., He, J., Fu, L., et al. (2017). Van der waals epitaxial growth of atomic layered HfS_2 crystals for ultrasensitive near-infrared phototransistors. Adv. Mater. 29, 1700439.

Gao, Y., Liu, Z.B., Sun, D.-M., Huang, L., Ma, L.-P., Yin, L.-C., Ma, T., Zhang, Z.Y., Ma, X.-L., Peng, L.-M., et al. (2015). Large-area synthesis of high-quality and uniform monolayer WS_2 on reusable Au foils. Nat. Commun. 6, 8569.

Gao, Y., Hong, Y.L., Yin, L.C., Wu, Z., Yang, Z., Chen, M.L., Liu, Z., Ma, T., Sun, D.M., Ni, Z., et al. (2017). Ultrafast growth of high-quality monolayer WSe_2 on Au. Adv. Mater. 29, 1700990.

Gaune-Escard, M., and Haarberg, G.M. (2014). Molten Salts Chemistry and Technology (John Wiley & Sons).

Geng, D.C., Zhao, X.X., Chen, Z.X., Sun, W.W., Fu, W., Chen, J.Y., Liu, W., Zhou, W., and Loh, K.P. (2017). Direct synthesis of large-area 2D Mo_2C on in situ grown graphene. Adv. Mater. 29, 1700072.

Hao, Y.F., Wang, L., Liu, Y.Y., Chen, H., Wang, X.H., Tan, C., Nie, S., Suk, J.W., Jiang, T.F., Liang, T.F., et al. (2016). Oxygen-activated growth and bandgap tunability of large single-crystal bilayer graphene. Nat. Nanotechnol. 11, 426–431.

Hu, D.K., Xu, G.C., Xing, L., Yan, X.X., Wang, J.Y., Zheng, J.Y., Lu, Z.X., Wang, P., Pan, X.Q., and Jiao, L.Y. (2017). Two-dimensional semiconductors grown by chemical vapor transport. Angew. Chem. Int. Ed. 56, 3611–3615.

Hu, X.Z., Huang, P., Jin, B., Zhang, X.W., Li, H.Q., Zhou, X., and Zhai, T.Y. (2018). Halide-induced self-limited growth of ultrathin nonlayered Ge flakes for high-performance phototransistors. J. Am. Chem. Soc. 140, 12909–12914.

Hu, D.K., Zhao, T.Q., Ping, X.F., Zheng, H.S., Xing, L., Liu, X.Z., Zheng, J.Y., Sun, L.F., Gu, L., Tao, C.G., et al. (2019). Unveiling the layer-dependent catalytic activity of $PtSe_2$ atomic crystals for the hydrogen evolution reaction. Angew. Chem. Int. Ed. 58, 6977–6981.

Huang, B., Clark, G., Navarro-Moratalla, E., Klein, D.R., Cheng, R., Seyler, K.L., Zhong, D., Schmidgall, E., McGuire, M.A., Cobden, D.H., et al. (2017). Layer-dependent ferromagnetism in a van der Waals crystal down to the monolayer limit. Nature 546, 270–273.

Huang, W.J., Gan, L., Yang, H.T., Zhou, N., Wang, R.Y., Wu, W.H., Li, H.Q., Ma, Y., Zeng, H.B., and Zhai, T.Y. (2017). Controlled synthesis of ultrathin 2D β-In_2S_3 with broadband photoresponse by chemical vapor deposition. Adv. Funct. Mater. 27, 1702448.

Ismach, A., Chou, H., Ferrer, D.A., Wu, Y.P., McDonnell, S., Floresca, H.C., Covacevich, A., Pope, C., Piner, R., Kim, M.J., et al. (2012). Toward

the controlled synthesis of hexagonal boron nitride films. ACS Nano 6, 6378–6385.

Ji, J.P., Song, X.F., Liu, J.Z., Yan, Z., Huo, C.X., Zhang, S.L., Su, M., Liao, L., Wang, W.H., Ni, Z.H., et al. (2016). Two-dimensional antimonene single crystals grown by van der Waals epitaxy. Nat. Commun. 7, 13352.

Ji, H.G., Lin, Y.-C., Nagashio, K., Maruyama, M., Solís-Fernández, P., Sukma Aji, A., Panchal, V., Okada, S., Suenaga, K., and Ago, H. (2018). Hydrogen-assisted epitaxial growth of monolayer tungsten disulfide and seamless grain stitching. Chem. Mater. 30, 403–411.

Jiang, S.L., Hong, M., Wei, W., Zhao, L.Y., Zhang, N., Zhang, Z.P., Yang, P.F., Gao, N., Zhou, X.B., Xie, C.Y., et al. (2018). Direct synthesis and in situ characterization of monolayer parallelogrammic rhenium diselenide on gold foil. Commun. Chem. 1, 17.

Jin, B., Huang, P., Zhang, Q., Zhou, X., Zhang, X.W., Li, L., Su, J.W., Li, H.Q., and Zhai, T.Y. (2018). Self-limited epitaxial growth of ultrathin nonlayered CdS flakes for high-performance photodetectors. Adv. Funct. Mater. 28, 1800181.

Ju, M., Liang, X.Y., Liu, J.X., Zhou, L., Liu, Z., Mendes, R.G., Rümmeli, M.H., and Fu, L. (2017). Universal substrate-trapping strategy to grow strictly monolayer transition metal dichalcogenides crystals. Chem. Mater. 29, 6095–6103.

Kim, H., Mattevi, C., Calvo, M.R., Oberg, J.C., Artiglia, L., Agnoli, S., Hirjibehedin, C.F., Chhowalla, M., and Saiz, E. (2012). Activation energy paths for graphene nucleation and growth on Cu. ACS Nano 6, 3614–3623.

Kim, K.K., Hsu, A., Jia, X.T., Kim, S.M., Shi, Y.M., Hofmann, M., Nezich, D., Rodriguez-Nieva, J.F., Dresselhaus, M., Palacios, T., et al. (2012). Synthesis of monolayer hexagonal boron nitride on Cu foil using chemical vapor deposition. Nano Lett. 12, 161–166.

Kong, D.S., Dang, W.H., Cha, J.J., Li, H., Meister, S., Peng, H.L., Liu, Z.F., and Cui, Y. (2010). Few-layer nanoplates of Bi_2Se_3 and Bi_2Te_3 with highly tunable chemical potential. Nano Lett. 10, 2245–2250.

Köppe, R., Steiner, J., and Schnöckel, H. (2003). GaP_5 und InP_5: Ungewöhnliche moleküle eröffnen neue wege zur reindarstellung von III/V-halbleitermaterialien. Z. Anorg. Allg. Chem. 629, 2168–2172.

Lei, S.D., Ge, L.H., Liu, Z., Najmaei, S., Shi, G., You, G., Lou, J., Vajtai, R., and Ajayan, P.M. (2013). Synthesis and photoresponse of large GaSe atomic layers. Nano Lett. 13, 2777–2781.

Li, X.S., Cai, W.W., An, J., Kim, S., Nah, J., Yang, D.X., Piner, R., Velamakanni, A., Jung, I., Tutuc, E., et al. (2009). Large-area synthesis of high-quality and uniform graphene films on copper foils. Science 324, 1312–1314.

Li, H.L., Duan, X.D., Wu, X.P., Zhuang, X.J., Zhou, H., Zhang, Q.L., Zhu, X.L., Hu, W., Ren, P.Y., Guo, P.F., et al. (2014). Growth of alloy $MoS_{2x}Se_{2(1-x)}$ nanosheets with fully tunable chemical compositions and optical properties. J. Am. Chem. Soc. 136, 3756–3759.

Li, S.S., Wang, S.F., Tang, D.-M., Zhao, W.J., Xu, H.L., Chu, L.Q., Bando, Y., Golberg, D., and Eda, G. (2015). Halide-assisted atmospheric pressure growth of large WSe_2 and WS_2 monolayer crystals. Appl. Mater. Today 1, 60–66.

Li, H.L., Zhang, Q.L., Duan, X.D., Wu, X.P., Fan, X.P., Zhu, X.L., Zhuang, X.J., Hu, W., Zhou, H., Pan, A.L., et al. (2015). Lateral growth of composition graded atomic layer $MoS_{2(1-x)}Se_{2x}$ nanosheets. J. Am. Chem. Soc. 137, 5284–5287.

Li, B., Huang, L., Zhao, G.Y., Wei, Z.M., Dong, H.L., Hu, W.P., Wang, L.-W., and Li, J.B. (2015). Large-size 2D β-Cu_2S nanosheets with giant phase transition temperature lowering (120 K) synthesized by a novel method of super-cooling chemical-vapor-deposition. Adv. Mater. 28, 8271–8276.

Li, Y., Duerloo, K.-A.N., Wauson, K., and Reed, E.J. (2016). Structural semiconductor-to-semimetal phase transition in two-dimensional materials induced by electrostatic gating. Nat. Commun. 7, 10671.

Li, P., Li, Z.Y., and Yang, J.L. (2017). Dominant kinetic pathways of graphene growth in chemical vapor deposition: the role of hydrogen. J. Phys. Chem. C 121, 25949–25955.

Li, J., Zhao, B., Chen, P., Wu, R.X., Li, B., Xia, Q.L., Guo, G.H., Luo, J., Zang, K.T., Zhang, Z.W., et al. (2018). Synthesis of ultrathin metallic MTe_2 (M = V, Nb, Ta) single-crystalline nanoplates. Adv. Mater. 30, 1801043.

Lin, M., Wu, D., Zhou, Y., Huang, W., Jiang, W., Zheng, W.S., Zhao, S.L., Jin, C.H., Guo, Y.F., Peng, H.L., et al. (2013). Controlled growth of atomically thin In_2Se_3 flakes by van der Waals epitaxy. J. Am. Chem. Soc. 135, 13274–13277.

Liu, L.X., Zhou, H.L., Cheng, R., Yu, W.J., Liu, Y., Chen, Y., Shaw, J., Zhong, X., Huang, Y., and Duan, X.F. (2012). High-yield chemical vapor deposition growth of high-quality large-area AB-stacked bilayer graphene. ACS Nano 6, 8241–8249.

Liu, J.X., Zeng, M.Q., Wang, L.X., Chen, Y.T., Xing, Z., Zhang, T., Liu, Z., Zuo, J.L., Nan, F., Mendes, R.G., et al. (2016). Ultrafast self-limited growth of strictly monolayer WSe_2 crystals. Small 12, 5741–5749.

Liu, L.N., Wu, J.X., Wu, L.Y., Ye, M., Liu, X.Z., Wang, Q., Hou, S.Y., Lu, P.F., Sun, L.F., Zheng, J.Y., et al. (2018). Phase-selective synthesis of 1T' MoS_2 monolayers and heterophase bilayers. Nat. Mater. 17, 1108–1114.

Liu, J.X., Zhou, L., Huang, K., Song, X.Y., Chen, Y.X., Liang, X.Y., Gao, J., Xiao, X.H., Rümmeli, M.H., and Fu, L. (2019). Regulation of two-dimensional lattice deformation recovery. iScience 13, 277–283.

Lu, G.Y., Wu, T.R., Yuan, Q.H., Wang, H.S., Wang, H.M., Ding, F., Xie, X.M., and Jiang, M.H. (2015). Synthesis of large single-crystal hexagonal boron nitride grains on Cu–Ni alloy. Nat. Commun. 6, 6160.

Ma, H.F., Chen, P., Li, B., Li, J., Ai, R.Q., Zhang, Z.W., Sun, G.Z., Yao, K.K., Lin, Z.Y., Zhao, B., et al. (2018). Thickness-tunable synthesis of ultrathin type-II dirac semimetal $PtTe_2$ single crystals and

their thickness-dependent electronic properties. Nano Lett. 18, 3523–3529.

Ma, H.F., Wan, Z., Li, J., Wu, R.X., Zhang, Z.W., Li, B., Zhao, B., Qian, Q., Liu, Y., Xia, Q.L., et al. (2019). Phase-tunable synthesis of ultrathin layered tetragonal CoSe and nonlayered hexagonal CoSe nanoplates. Adv. Mater. 31, 1900901.

Mak, K.F., Lee, C.G., Hone, J., Shan, J., and Heinz, T.F. (2010). Atomically thin MoS$_2$: a new direct-gap semiconductor. Phy. Rev. Lett. 105, 136805.

Manukyan, K.V., Kirakosyan, K.G., Grigoryan, Y.G., Niazyan, O.M., Yeghishyan, A.V., Kirakosyan, A.G., and Kharatyan, S.L. (2011). Mechanism of molten-salt-controlled thermite reactions. Ind. Eng. Chem. Res. 50, 10982–10988.

Naylor, C.H., Parkin, W.M., Ping, J.L., Gao, Z.L., Zhou, Y.R., Kim, Y., Streller, F., Carpick, R.W., Rappe, A.M., Drndić, M., et al. (2016). Monolayer single-crystal 1T′-MoTe$_2$ grown by chemical vapor deposition exhibits weak antilocalization effect. Nano Lett. 16, 4297–4304.

Ohta, T., Bostwick, A., Seyller, T., Horn, K., and Rotenberg, E. (2006). Controlling the electronic structure of bilayer graphene. Science 313, 951–954.

Shi, J.P., Wang, X.N., Zhang, S., Xiao, L.F., Huan, Y.H., Gong, Y., Zhang, Z.P., Li, Y.C., Zhou, X.B., Hong, M., et al. (2017). Two-dimensional metallic tantalum disulfide as a hydrogen evolution catalyst. Nat. Commun. 8, 958.

Shi, J.P., Chen, X.X., Zhao, L.Y., Gong, Y., Hong, M., Huan, Y.H., Zhang, Z.P., Yang, P.F., Li, Y., Zhang, Q.H., et al. (2018). Chemical vapor deposition grown wafer-scale 2D tantalum diselenide with robust charge-density-wave order. Adv. Mater. 30, 1804616.

Splendiani, A., Sun, L., Zhang, Y.B., Li, T.S., Kim, J., Chim, C.-Y., Galli, G., and Wang, F. (2010). Emerging photoluminescence in monolayer MoS$_2$. Nano Lett. 10, 1271–1275.

Suenaga, K., Ji, H.G., Lin, Y.-C., Vincent, T., Maruyama, M., Aji, A.S., Shiratsuchi, Y., Ding, D., Kawahara, K., Okada, S., et al. (2018). Surface-mediated aligned growth of monolayer MoS$_2$ and in-plane heterostructures with graphene on sapphire. ACS Nano 12, 10032–10044.

Sung, J.H., Heo, H., Si, S., Kim, Y.H., Noh, H.R., Song, K., Kim, J., Lee, C.-S., Seo, S.-W., Kim, D.-H., et al. (2017). Coplanar semiconductor–metal circuitry defined on few-layer MoTe$_2$ via polymorphic heteroepitaxy. Nat. Nanotechnol. 12, 1064–1070.

Susarla, S., Kutana, A., Hachtel, J.A., Kochat, V., Apte, A., Vajtai, R., Idrobo, J.C., Yakobson, B.I., Tiwary, C.S., and Ajayan, P.M. (2017). Quaternary 2D transition metal dichalcogenides (TMDs) with tunable bandgap. Adv. Mater. 29, 1702457.

Tay, R.Y., Griep, M.H., Mallick, G., Tsang, S.H., Singh, R.S., Tumlin, T., Teo, E.H.T., and Karna, S.P. (2014). Growth of large single-crystalline two-dimensional boron nitride hexagons on electropolished copper. Nano Lett. 14, 839–846.

Voiry, D., Mohite, A., and Chhowalla, M. (2015). Phase engineering of transition metal dichalcogenides. Chem. Soc. Rev. 44, 2702–2712.

Wang, H., Wang, G.Z., Bao, P.F., Yang, S.L., Zhu, W., Xie, X., and Zhang, W.-J. (2012). Controllable synthesis of submillimeter single-crystal monolayer graphene domains on copper foils by suppressing nucleation. J. Am. Chem. Soc. 134, 3627–3630.

Wang, J., Zeng, M.Q., Tan, L.F., Dai, B.Y., Deng, Y., Rummeli, M., Xu, H.T., Li, Z.S., Wang, S., Peng, L.M., et al. (2013). High-mobility graphene on liquid p-block elements by ultra-low-loss CVD growth. Sci. Rep. 3, 2670–2676.

Wang, J.Y., Zheng, H.S., Xu, G.C., Sun, L.F., Hu, D.K., Lu, Z.X., Liu, L.N., Zheng, J.Y., Tao, C.G., and Jiao, L.Y. (2016). Controlled synthesis of two-dimensional 1T-TiSe$_2$ with charge density wave transition by chemical vapor transport. J. Am. Chem. Soc. 138, 16216–16219.

Wang, Z.Q., Liu, P., Ito, Y., Ning, S.C., Tan, Y.W., Fujita, T., Hirata, A., and Chen, M.W. (2016). Chemical vapor deposition of monolayer Mo$_{1-x}$W$_x$S$_2$ crystals with tunable band gaps. Sci. Rep. 6, 21536.

Wang, H., Huang, X.W., Lin, J.H., Cui, J., Chen, Y., Zhu, C., Liu, F.C., Zeng, Q.S., Zhou, J.D., Yu, P., et al. (2017). High-quality monolayer superconductor NbSe$_2$ grown by chemical vapour deposition. Nat. Commun. 8, 394.

Wang, D.G., Zhang, X.W., Guo, G.C., Gao, S.H., Li, X.X., Meng, J.H., Yin, Z.G., Liu, H., Gao, M.L., Cheng, L.K., et al. (2018). Large-area synthesis of layered HfS$_{2(1-x)}$Se$_{2x}$ alloys with fully tunable chemical compositions and bandgaps. Adv. Mater. 30, 1803285.

Wang, F.K., Gao, T., Zhang, Q., Hu, Z.-Y., Jin, B., Li, L., Zhou, X., Li, H.Q., Van Tendeloo, G., and Zhai, T.Y. (2019). Liquid-alloy-assisted growth of 2D ternary Ga$_2$In$_4$S$_9$ toward high-performance UV photodetection. Adv. Mater. 31, 1806306.

Wen, Y., Wang, Q.S., Yin, L., Liu, Q., Wang, F., Wang, F.M., Wang, Z.X., Liu, K.L., Xu, K., Huang, Y., et al. (2016). Epitaxial 2D PbS nanoplates arrays with highly efficient infrared response. Adv. Mater. 28, 8051–8057.

Wu, P., Zhang, W.H., Li, Z.Y., and Yang, J.L. (2014). Mechanisms of graphene growth on metal surfaces: theoretical perspectives. Small 10, 2136–2150.

Wu, J.X., Yuan, H.T., Meng, M.M., Chen, C., Sun, Y., Chen, Z.Y., Dang, W.H., Tan, C.W., Liu, Y.J., Yin, J.B., et al. (2017). High electron mobility and quantum oscillations in non-encapsulated ultrathin semiconducting Bi$_2$O$_2$Se. Nat. Nanotechnol. 12, 530–534.

Xie, L.M. (2015). Two-dimensional transition metal dichalcogenide alloys: preparation, characterization and applications. Nanoscale 7, 18392–18401.

Xu, C., Wang, L.B., Liu, Z.B., Chen, L., Guo, J.K., Kang, N., Ma, X.-L., Cheng, H.-M., and Ren, W.C. (2015). Large-area high-quality 2D ultrathin Mo$_2$C superconducting crystals. Nat. Mater. 14, 1135–1141.

Xu, D., Chen, W.Y., Zeng, M.Q., Xue, H.F., Chen, Y.X., Sang, X.H., Xiao, Y., Zhang, T., Unocic, R.R., Xiao, K., et al. (2018). Crystal-field tuning of photoluminescence in two-dimensional materials with embedded lanthanide ions. Angew. Chem. Int. Ed. 57, 755–759.

Yang, P.F., Zou, X.L., Zhang, Z.P., Hong, M., Shi, J.P., Chen, S.L., Shu, J.P., Zhao, L.Y., Jiang, S.L., Zhou, X.B., et al. (2018). Batch production of 6-inch uniform monolayer molybdenum disulfide catalyzed by sodium in glass. Nat. Commun. 9, 979.

Yang, D., Hu, X.Z., Zhuang, M.H., Ding, Y., Zhou, S.S., Li, A.J., Yu, Y.W., Li, H.Q., Luo, Z.T., Gan, L., et al. (2018). Inversion symmetry broken 2D 3R-MoTe$_2$. Adv. Funct. Mater. 28, 1800785.

Yao, K.K., Chen, P., Zhang, Z.W., Li, J., Ai, R.Q., Ma, H.F., Zhao, B., Sun, G.Z., Wu, R.X., Tang, X.W., et al. (2018). Synthesis of ultrathin two-dimensional nanosheets and van der Waals heterostructures from non-layered γ-CuI. npj 2D Mater. Appl. 2, 16.

Yazyev, O.V., and Louie, S.G. (2010). Electronic transport in polycrystalline graphene. Nat. Mater. 9, 806–809.

Yu, Q.K., Lian, J., Siriponglert, S., Li, H., Chen, Y.P., and Pei, S.-S. (2008). Graphene segregated on Ni surfaces and transferred to insulators. Appl. Phys. Lett. 93, 113103.

Zeng, M.Q., and Fu, L. (2018). Controllable fabrication of graphene and related two-dimensional materials on liquid metals via chemical vapor deposition. Acc. Chem. Res. 51, 2839–2847.

Zeng, M.Q., Chen, Y.X., Zhang, E.Z., Li, J.X., Mendes, R.G., Sang, X.H., Luo, S.L., Ming, W.M., Fu, Y.H., Du, M.-H., et al. (2019). Molecular scaffold growth of two-dimensional, strong interlayer-bonding-layered materials. CCS Chem. 1, 117–127.

Zhang, Y.B., Tang, T.-T., Girit, C., Hao, Z., Martin, M.C., Zettl, A., Crommie, M.F., Shen, Y.R., and Wang, F. (2009). Direct observation of a widely tunable bandgap in bilayer graphene. Nature 459, 820–823.

Zhang, X.Y., Li, H., and Ding, F. (2014). Self-assembly of carbon atoms on transition metal surfaces-chemical vapor deposition growth mechanism of graphene. Adv. Mater. 26, 5488–5495.

Zhang, W.T., Li, X.D., Jiang, T.T., Song, J.L., Lin, Y., Zhu, L.X., and Xu, X.L. (2015). CVD synthesis of Mo$_{(1-x)}$W$_x$S$_2$ and MoS$_{2(1-x)}$Se$_{2x}$ alloy monolayers aimed at tuning the bandgap of molybdenum disulfide. Nanoscale 7, 13554–13560.

Zhang, M., Zhu, Y.M., Wang, X.S., Feng, Q.L., Qiao, S.L., Wen, W., Chen, Y.F., Cui, M.H., Zhang, J., Cai, C.Z., et al. (2015). Controlled synthesis of ZrS$_2$ monolayer and few layers on hexagonal boron nitride. J. Am. Chem. Soc. 137, 7051–7054.

Zhang, Z.P., Niu, J.J., Yang, P.F., Gong, Y.F., Ji, Q.Q., Shi, J.P., Fang, Q.Y., Jiang, S.L., Li, H., Zhou, X.B., et al. (2017). Van der Waals epitaxial growth of 2D metallic vanadium diselenide single crystals and their extra-high electrical conductivity. Adv. Mater. 29, 1702359.

Zhang, Q.Q., Xiao, Y., Zhang, T., Weng, Z., Zeng, M.Q., Yue, S.L., Mendes, R.G., Wang, L.X., Chen, S.L., Rümmeli, M.H., et al. (2017). Iodine-mediated chemical vapor deposition growth of

metastable transition metal dichalcogenides. Chem. Mater. *29*, 4641–4644.

Zhang, X.M., Nan, H.Y., Xiao, S.Q., Wan, X., Gu, X.F., Du, A.J., Ni, Z.H., and Ostrikov, K.K. (2019). Transition metal dichalcogenides bilayer single crystals by reverse-flow chemical vapor epitaxy. Nat. Commun. *10*, 598.

Zhang, Y., Chu, J.W., Yin, L., Shifa, T.A., Cheng, Z.Z., Cheng, R.Q., Wang, F., Wen, Y., Zhan, X.Y., Wang, Z.X., et al. (2019). Ultrathin magnetic 2D single-crystal CrSe. Adv. Mater. *31*, 1900056.

Zhao, S.L., Wang, H., Zhou, Y., Liao, L., Jiang, Y., Yang, X., Chen, G.C., Lin, M., Wang, Y., Peng, H.L., et al. (2015). Controlled synthesis of single-crystal SnSe nanoplates. Nano Res. *8*, 288–295.

Zhao, B., Dang, W.Q., Liu, Y., Li, B., Li, J., Luo, J., Zhang, Z.W., Wu, R.X., Ma, H.F., Sun, G.Z., et al.

(2018). Synthetic control of two-dimensional NiTe$_2$ single crystals with highly uniform thickness distributions. J. Am. Chem. Soc. *140*, 14217–14223.

Zhou, H.L., Yu, W.J., Liu, L.X., Cheng, R., Chen, Y., Huang, X.Q., Liu, Y., Wang, Y., Huang, Y., and Duan, X.F. (2013). Chemical vapour deposition growth of large single crystals of monolayer and bilayer graphene. Nat. Commun. *4*, 2096.

Zhou, Y.H., Nie, Y.F., Liu, Y.J., Yan, K., Hong, J.H., Jin, C.H., Zhou, Y., Yin, J.B., Liu, Z.F., and Peng, H.L. (2014). Epitaxy and photoresponse of two-dimensional GaSe crystals on flexible transparent mica sheets. ACS Nano *8*, 1485–1490.

Zhou, X., Gan, L., Tian, W.M., Zhang, Q., Jin, S.Y., Li, H.Q., Bando, Y., Golberg, D., and Zhai, T.Y. (2015). Ultrathin SnSe$_2$ flakes grown by chemical

vapor deposition for high-performance photodetectors. Adv. Mater. *27*, 8035–8041.

Zhou, J.D., Zeng, Q.S., Lv, D.H., Sun, L.F., Niu, L., Fu, W., Liu, F.C., Shen, Z.X., Jin, C.H., and Liu, Z. (2015). Controlled synthesis of high-quality monolayered alpha-In$_2$Se$_3$ via physical vapor deposition. Nano Lett. *15*, 6400–6405.

Zhou, J.D., Lin, J.H., Huang, X.W., Zhou, Y., Chen, Y., Xia, J., Wang, H., Xie, Y., Yu, H.M., Lei, J.C., et al. (2018). A library of atomically thin metal chalcogenides. Nature *556*, 355–359.

Zhou, S.S., Wang, R.Y., Han, J.B., Wang, D.L., Li, H.Q., Gan, L., and Zhai, T.Y. (2019). Ultrathin non-van der Waals magnetic rhombohedral Cr$_2$S$_3$: space-confined chemical vapor deposition synthesis and Raman scattering investigation. Adv. Funct. Mater. *29*, 1805880.